Scanning Microscopy

Volume 9 | Number 2 Article 5

5-25-1995

Cathodoluminescence Contrast of Localized Defects Part II. Defect Investigation

K. L. Pey
National University of Singapore

J. C. H. Phang
National University of Singapore

D. S. H. Chan
National University of Singapore

Scanning Microscopy, Vol. 9, No. 2, 1995 (Pages 367-380) 0891-7035/95$5.00+.25
Scanning Microscopy International, Chicago (AMF O'Hare), IL 60666 USA

CATHODOLUMINESCENCE CONTRAST OF LOCALIZED DEFECTS PART II. DEFECT INVESTIGATION

K.L. Pey, J.C.H. Phang and D.S.H. Chan*

Centre for Integrated Circuit Failure Analysis and Reliability, Faculty of Engineering
National University of Singapore, 10 Kent Ridge Crescent, Singapore 0511

(Received for publication June 1, 1994, and in revised form May 25, 1995)

Abstract

Cathodoluminescence contrast from defects with different geometrical and electronic properties have been studied using the numerical model developed in Part I. The contrast of a localized subsurface defect exhibits a maxima at a specific beam energy E_{max} which corresponds to the depth of the defect. The contrast of a dislocation which intersects the top surface perpendicularly is a decreasing function of beam energy. The differences in the image profiles of the two different kinds of defects allow the two types of imperfections to be distinguished. In addition, the resolution of a subsurface defect at beam energies lower than E_{max} is only a function of defect size and is insensitive to the defect strength. The defect depth, size and strength can therefore be extracted sequentially. The extension of the model to the investigation of complex or multiple defects such as "dot and halo" contrast is also illustrated.

Key Words: Cathodoluminescence, cathodoluminescence contrast, defects, scanning electron microscope, semiconductors, dislocations, subsurface defects.

*Address for correspondence:
DSH Chan
Department of Electrical Engineering
National University of Singapore
10 Kent Ridge Crescent, Singapore 0511
Telephone Number: (65) 772-2132
FAX Number: (65) 779-1103

Introduction

In the defect study using cathodoluminescence (CL) [3, 11, 12, 13], different mathematical descriptions for the defect geometries and properties have been formulated to model the contrast mechanism. However, mathematically, it is very difficult to extend these models to investigate CL response in the presence of complex or multiple defects.

In this paper, the CL model developed in an earlier paper, hereafter called CL Model, is applied to simulate contrasts from defects in CL images. The contrast profiles of subsurface localized defects, dislocations which intersect the top surface perpendicularly and "dot and halo" responses in GaAs materials are determined. Arising from the difference in the contrast behaviour in CL images, a method for differentiating dislocations and bulk defects based only on the energy dependent CL contrast is suggested. It will be shown that by locating the beam energy at which maximum CL contrast occurs, the depth of a bulk defect can be obtained. The applications of the model to the extraction of other defect parameters are also discussed.

Cathodoluminescence Contrast from Defects

Cathodoluminescence contrast from a single defect

Booker [2], Löhnert and Kubalek [12], Holt and Saba [9], and Pasemann and Hergert [14] reviewed the analysis of CL contrast produced by dislocations. The CL contrast may be defined as

$$C(t,E) = \frac{I_{CL(t,E)} - I_{CL(\infty,E)}}{I_{CL(\infty,E)}} \qquad (1)$$

where $I_{CL(\infty,E)}$ and $I_{CL(t,E)}$ are, respectively, the CL intensities far away from any defect and at a distance t from the centre of the defect of interest (Fig. 1 of Part I). The contrast is also a function of beam energy E.

For a defect free region, the CL intensity can be expressed as

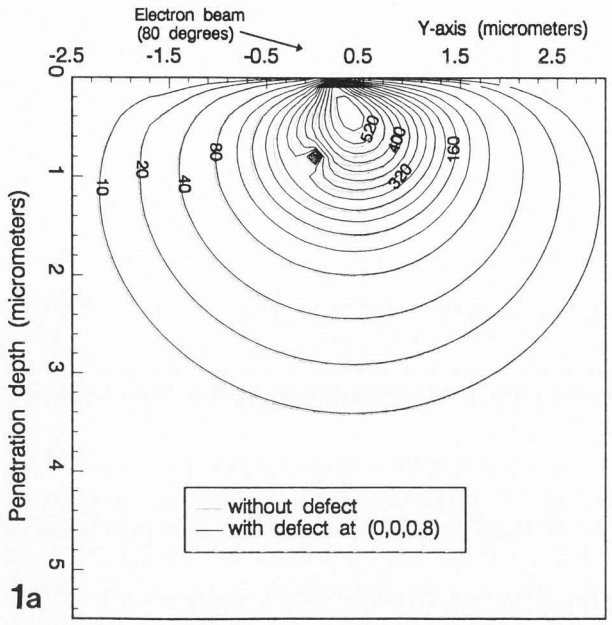

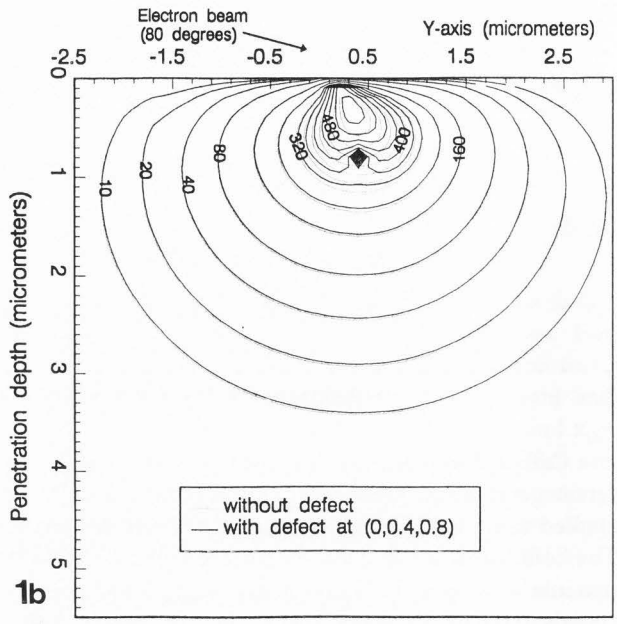

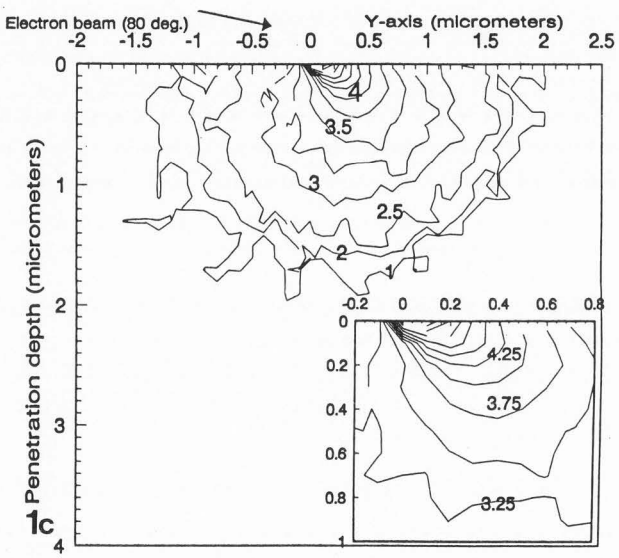

Figure 1. Carrier concentration contours in cm^{-3} with and without a point defect of strength $\gamma(r) = 1479\ \mu m^{-2}$ (a) at (0, 0, 0.8 μm) (b) at (0, 0.4 μm, 0.8 μm). (c) Energy dissipation contours in 10^n ev/μm^3. Electron in GaAs at x = 0 for a 20 keV electron beam with $\theta_o = 80°$. Other parameters are normalized surface recombination velocity $V_s \rightarrow \infty$, radius of the incident electron beam $\delta = 0\ \mu m$, D = 1 x 10^9 μm^2/sec, beam current = 1 nA, $\tau'_{nr}/\tau'_r = 1/2000$, $\tau_r/\tau'_r = 1$ and $\tau'_{nr} \gg \tau'_r$.

$$I_{CL(\infty,E)} = \int_{\Omega_s} \frac{A'(z)p_o(r)}{\tau_r} d^3r \qquad (2)$$

where $p_o(r)$ is the excess minority carrier concentration in the defect free region, Ω_s denotes the sample volume and A'(z) is the function containing the optical losses due to self-absorption and reflection losses. The photon flux in the presence of a defect is [14]

$$I_{CL(t,E)} = \int_{\Omega_s} \frac{A'(z)p(r)}{\tau_r} d^3r + \left[\frac{1}{\tau'_r} - \frac{1}{\tau_r}\right] \int_{\Omega_d} A'(z)p(r)d^3r \qquad (3)$$

where Ω_d denotes the volume of the defect characterized by a radiative lifetime τ'_r and non-radiative lifetime τ'_{nr}, each of which differs from the corresponding τ_r and τ_{nr} outside the defect region. i.e.,

$$\tau = (\tau_r\tau_{nr}) / (\tau_r + \tau_{nr}) \qquad (4)$$

$$\tau' = (\tau'_r\tau'_{nr}) / (\tau'_r + \tau'_{nr}) \qquad (5)$$

Substituting eqs. (2) and (3) into eq. (1), the CL contrast becomes

$$C(t,E) = \frac{\int_{\Omega_s} A'(z)p(r)d^3r}{\tau_r I_{CL(\infty,E)}} + \frac{\left[\frac{\tau_r}{\tau'_r} - 1\right] \int_{\Omega_d} A'(z)p(r)d^3r}{\tau_r I_{CL(\infty,E)}} - 1 \qquad (6)$$

The first term on the right-hand side of eq. (6) arises from the change in p(r) due to the difference

between τ and τ'. In such cases, the CL contrast is similar to EBIC contrast. The second component is due to the effect of changes in the radiative lifetime only and is present only in the CL mode but not in the EBIC mode.

With reference to Figure 1 of Part I, it can be observed that if F falls on the plane x = 0 and reduces to a point or a threading line, the physical situation becomes symmetrical about the Y-axis, since g(r) will in any case, even for $\theta_o > 0°$, have at least bi-axial symmetry about the Y-axis. So one can suppose that the beam moves along the Y-axis and now t has only the y-component.

Two important parameters are defined for a contrast profile. The "maximum contrast" of a contrast profile is denoted by

$$C(E) = \left| \textit{maximum } C(t,E) \right| \tag{7}$$

and the resolution of a CL image will be defined as the full-width half minimum, W(E) of C(t,E). For $\theta_o = 0°$ and by symmetry, C(E) occurs at y = 0. W(E) gives a measure of the precision that is possible when locating the defect on the X-Y plane, while C(E) is related to the depth of a subsurface defect.

Implementation in the cathodoluminescence model of Part I

CL contrast can be a function of both non-radiative and radiative lifetimes (eq.(6)). In this work, the radiative lifetime is assumed to be constant throughout the material, and only the non-radiative lifetime varies with position in the material. As a result, eq. (6) can be simplified to

$$C(t,E) = \frac{\int_{\Omega_s} A'(z)p(r)d^3r}{\tau_r I_{CL(\infty,E)}} - 1 \tag{8}$$

In the actual implementation, the existence of a defect in the CL Model is controlled by γ_{oi} and e_{oi} of eq. (18) of Part I. In the case of a defect free situation, γ_{oi} and e_{oi} associated with all the nodes defined by the central finite difference scheme are set to zero, i.e., these parameters do not spatially vary. The presence of a defect is modelled by putting γ_{oi} and e_{oi} of those nodes that are bound by the defect region to a non-zero value. The geometrical parameters of the lattice imperfections such as size, shape and depth are controlled through the parameter e_{oi}. The defect strength is characterized by the parameter γ_{oi} and defined by eq. (3) of Part I.

The modelling of defects with arbitrary shapes and sizes can hence be easily realized through this approach. For example, a point lattice imperfection is modelled by a node which has a non-zero e_{oi} and γ_{oi} in the three-dimensional space. Similarly, a one-dimensional threading defect can be treated as a series of nodes with non-zero e_{oi} and γ_{oi} connected in the form of a chain. This scheme also provides the flexibility in implementing other irregular defects with different kinds of geometrical properties.

In summary, the following steps have been adopted in the CL Model to obtain a CL contrast profile across a defect location:

(1) The Monte Carlo method is used to model the electron energy dissipation distribution in semiconductors, and the data is stored;

(2) The grid spacings and sample volume of interest are produced for a given set of simulation parameters, taking into consideration all the cell partitioning criteria in Part I;

(3) The input parameters together with the Monte Carlo results and the set of associated meshes are fed into the numerical model to calculate the distribution of minority carrier concentrations at each node in the defined three dimensional space using eq. (18) of Part I;

(4) The amount of photon flux which has escaped from the exit surface is evaluated using the numerical method described in Part I and the formulae developed in Phang *et al.* [16]. The overall intensity $I_{CL(t,E)}$ is hence calculated;

(5) Steps 2 to 4 are repeated for other values of t to obtain a series of $I_{CL(t,E)}$ values; and

(6) Eq. (8) is applied to obtain the CL contrast as a function of t.

Cathodoluminescence contrast from multiple defects

Mathematically, it is very tedious to extend Donolato's EBIC model [6] and Jakubowicz's CL model [11] to investigate CL contrast in the presence of multiple defects or lattice imperfections with complicated geometries such as the well known "dot and halo" [18] response. Obtaining the exact analytical solution for such situations is almost impossible or may require the solving of integrals containing Green's function of the geometry such as eq. (10) of [6].

The formulation of CL contrast from defects normally requires only the knowledge of the excess carrier density distribution. Pasemann and Hergert [14], Löhnert and Kubalek [12] and Jakubowicz [11] have derived analytical expressions for the case of point defects, and dislocations with different inclination angles to the top surface. But these are limited to the case of a single defect with simple geometry. For multiple defect geometries, the interactions among defects and the different influences of each of the defects complicate the derivation of the distribution of excess minority carrier density. As pointed out by Jakubowicz [11], "an exact treatment of the problem would require the consideration of interactions between the individual defects." The approximation normally used for extended defects such as

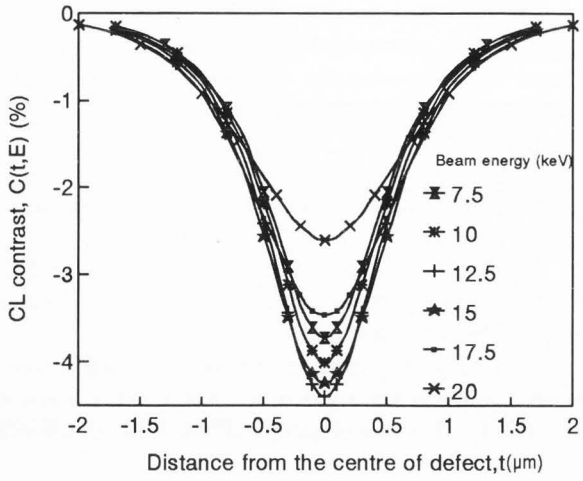

Figure 2. CL contrast profiles for various values of beam energies for a point defect of strength $\gamma(r) = 1479$ μm^{-2} located at d = 0.8 μm in GaAs. Other relevant parameters are $\theta_o = 0°$, $\delta = 0$ μm, $V_s \rightarrow \infty$, L = 1 μm, the optical absorption coefficient $\alpha = 0.1$ μm^{-1}, $\gamma(r) = 1479$ μm^{-2}, D = 1 x 10^9 μm^2/sec, beam current = 1 nA, $\tau'_{nr}/\tau'_r = 1/2000$, $\tau_r/\tau'_r = 1$ and $\tau'_{nr} \gg \tau'_r$.

---

dislocations is to combine point defects with the **same strength** and to take into account interactions of the first order between point defects only [11].

However, these problems can be overcome by the proposed method in a straightforward manner. In the present model, the interactions among the defects and other complicated factors have been implicitly taken care of by the sets of finite difference equations at the nodes. As such, eq. (8) can be extended to more complicated situations where p(r) is the minority carrier density produced by a beam in the presence of multiple defects.

Effect of a Point Defect on Cathodoluminescence Contrast

Dependence of carrier distribution on defects

In this work, the defect is assumed to act as a sink for excess minority carriers, similar to the non-radiative surface recombination velocity. The stronger the defect strength or the larger the size, the more e-h pairs will be eliminated non-radiatively at and in the vicinity of the defect region. An interesting situation is the effect of incident beam angle on the distribution of p(r) in GaAs with and without a point defect. Figures 1a and 1b illustrate two examples with point defects located at (0.0 μm, 0.0 μm, 0.8 μm) and (0.0 μm, 0.4 μm, 0.8 μm) respectively. The e-h pair source for these curves is shown in Figure 1c. As a result of the large off-normal

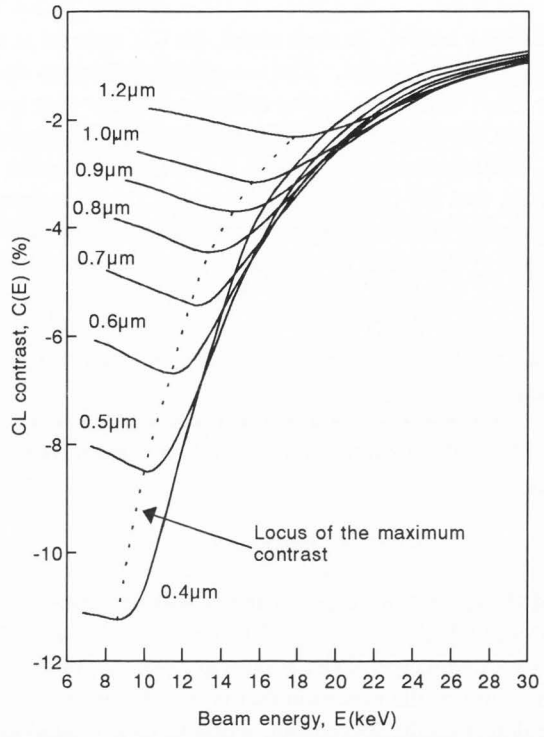

Figure 3. C(E) profiles for point defects located at different depths.

---

incidence (80°) of the electron beam, the maximum p(r) region is shifted into the positive region of the Y-axis. The symmetry of the profiles about the X-axis is no longer present. Due to this property, the defect located at y = 0.4 μm appears to have a larger influence on p(r) since the energy dissipation profiles are tilted more towards the defect as compared to the defect at y = 0 μm. It can be predicted that the CL contrast profile for off-normal incident beam will be tilted.

Dependence of contrast profiles on defect parameters

Three parameters of the defect are crucial for defect contrast:

(1) The depth d of the defect;

(2) The radius or size Wd of the defect;

(3) The density of the recombination centres and the characteristics of the recombination process. Both of these can be modelled through $\gamma(r)$.

Jakubowicz [10] only considered factors (2) and (3) and found that two defects having different combinations of values of (2) and (3) can appear to be defects of the same "strength" when viewed using EBIC. The definition of defect strength by Jakubowicz [10] includes defect parameters (2) and (3). Since CL is a related phenomenon of EBIC in the SEM, the same prediction can be postulated for defect contrast in CL images. It is believed that the depth of defect also plays an important role in the contrast observed, and hence, it is listed as one of the parameters of interest for the present study.

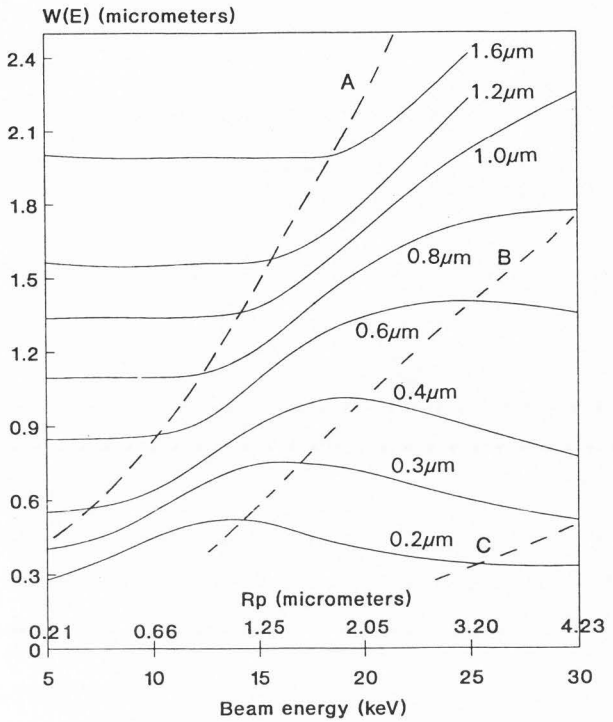

Figure 4. W(E) profiles for point defects located at different depths. Curve (1) d = 0.2 μm (2) d = 0.3 μm (3) d = 0.4 μm (4) d = 0.6 μm (5) d = 0.8 μm (6) d = 1.0μm (7) d = 1.2 μm (8) d = 1.6 μm. Curve (A) E = LT_{bv} and $R_p \approx$ d, curve (B) is the worst condition to observe the defect, curve (C) E = HT_{bv}.

Effect of defect depth

Figure 2 gives contrast responses for a bulk point defect located at a depth, d = 0.8 μm in GaAs. These curves show that with increasing beam energy, the magnitude of C(E) (i.e., contrasts at t = 0) of the contrast profiles goes through a maximum; in contrast, W(E) of the curves shows only minor variations up to about 12.5 keV. However, for higher beam energies, the profiles broaden considerably (see curve 5 of Fig. 4).

To study the influence of defect depth on contrast profiles in greater detail, results similar to those in Figure 2 of other subsurface point defects located at various depths ranging from 0.2 μm to 1.6 μm under the same conditions were investigated. Figure 3 shows C(E) for selected values of d. From the plots, it can be observed that:

(1) All curves exhibit a maximum contrast, $C(E)_{max}$. This maximum contrast in each curve occurs at a specific beam energy, E_{max}, which corresponds to a particular d;

(2) As for the dependence on d, $C(E)_{max}$ decreases rapidly with d. Therefore the selection of the appropriate energy range for locating $C(E)_{max}$ is important; shallower defects require a low beam energy range and vice versa;

(3) The contrast discrimination is good for shallow defects with d ranging from 0.2 μm to 0.6 μm. As d increases, the contrast discrimination becomes poorer, which results in a higher error when locating the maximum contrast.

Figure 4 shows the resolution curves corresponding to the contrasts in Figure 3 for L = 1 μm. R_p is the maximum penetration range determined by the Monte Carlo calculation for normal incidence of electrons and is shown on the bottom scale of the graph for the corresponding beam energy. Basically all curves can be broken down into four regions:

Region I. $R_p \leq$ d(see particularly curves 4-8): in this region, W(E) stays almost constant until E reaches a low threshold beam voltage (LT_{bv}), denoted by the dotted curve A on which $R_p \approx$ d;

Region II. d < $R_p \leq$ 5d-6d: this region starts from the LT_{bv} to the beam energy for the maximum W(E) and has the worst resolution. In this area, with increasing E, the width increases and reaches the worst resolution for observing that particular defect. Dotted curve B gives the locus for the worst resolution for different values of d;

Region III. 5d-6d < $R_p \leq$ 15d-16d: within this region, W(E) decreases gradually with E until E meets the high threshold beam voltage HT_{bv} (dotted curve C);

Region IV. $R_p >>$ d: this begins from HT_{bv} and goes to higher beam energies. W(E) of this region appears to be constant again, however, it stabilizes at a value higher than that of Region I.

Over the entire four regions, there is no distinctive minimum in W(E) for a particular defect depth. However, Donolato [6] found that for EBIC, a minimum occurs when $R_p \approx$ 1.04a, where a is the depth of the defect. It may be possible that for CL, in addition to these four regions, there is another region to the left of Region I (where d >> R_p, see curves 7 and 8 at low beam energies). In this region, it is possible that W(E) will increase with decreasing E. Interestingly, Regions I, III and IV are not present in Donolato's EBIC model [6] for subsurface localized defects in which a uniform generation sphere with diameter R_p was assumed. However, it can be argued that Regions III and IV can still be observed if one sets $R_p >$ 5d-6d in his model.

An approach for estimating the resolution of CL images can be made based on Figure 4[1]. The best resolution that can be achieved is W(E) $\approx$ 1.33d in Region I.

---

[1]Although the results presented are for L = 1 μm and α = 0.1 μm^{-1}, the discussions can be extended to other values of L and α.

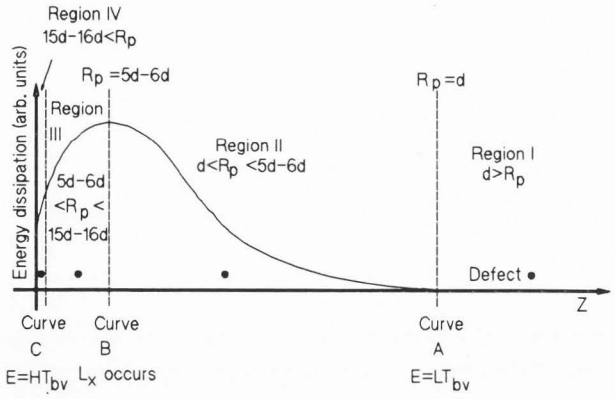

Figure 5. Schematic illustration of the interaction of a depth dose curve with subsurface point defects located at different depths.

For $d < R_p \leq$ 15d-16d, i.e., Regions II and III, the resolution has an upper limit value of W(E) $\approx$ 2.6d, while for $R_p >$ 15d-16d, W(E) is approximately 1.6d. The parameters d and R_p play an important role in deciding the image resolution; for Regions I and II, W(E) is basically controlled by d or R_p, whichever is greater; for Region IV, d is the only deciding parameter; for Region III, both factors have a negligible effect on W(E). In addition, it is worthwhile to note that the effect of d on W(E) is that the half-width values are greater for higher values of d for a specific E.

As an explanation to the mechanism for W(E) variations with beam energy, one may construct a diagram as shown in Figure 5 which is helpful for visualizing the interactions between d and the generation function of the incident electrons. Although the case where d = 0.4 μm will be analyzed in detail, the argument is valid for any other defect depths. Also, it must be noted that R_p is indirectly related to the lateral width L_x of the e-h pair source since higher beam energies will result in larger values of R_p and L_x. Similar to Figure 4, four main regions are defined in Figure 5:

Region I. $R_p \leq d = 0.4$ μm, e.g., E = 5 keV: R_p and L_x have negligible effect on W(E) since the defect location is outside the generation volume. When the beam energy is equal to LT_{bv} ($\approx$ 7.5 keV), $d \approx R_p$;

Region II. $d < R_p <$ 5d-6d, e.g., 7.5 keV < E < 20 keV: W(E) is an increasing function of E, since the defect now falls within the generation profiles when the beam comes sufficiently close to it and interacts more strongly with the e-h pairs. Effect of the lateral spreading broadens W(E). At $R_p \approx$ 5d-6d, according to the Monte Carlo results, the depth of the defect coincides with the depth for the maximum energy dissipation. To a good approximation, this is also the position where the maximum L_x appears. The depth

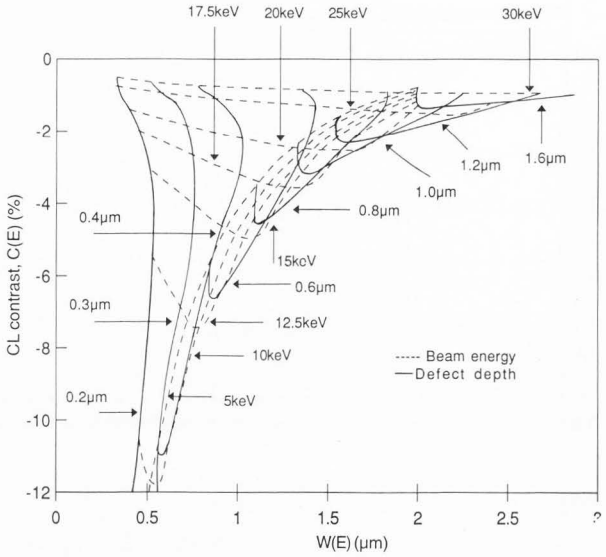

Figure 6. Plot of C(E) versus W(E) of point defects for different defect depths; Wd $\rightarrow$ 0 μm and $\gamma(r) = 1479$ μm^{-2}.

---

dose and carrier concentration contours of a Monte Carlo calculation for a 20 keV electron beam confirm this observation for z = d = 0.4 μm. As a result, this gives rise to the worst resolution of the CL micrographs;

Region III. 5d-6d < R_p < 15d-16d, e.g., 20 keV < E < 30 keV: the effect is similar to region two but is in the reverse order. W(E) decreases with E, and this is probably due to the defect moving further away from the position for maximum energy dissipation and L_x;

Region IV. $R_p >$ 15d-16d: the defect is located very near the top surface compared to the value of R_p. The effect of R_p and L_x on W(E) is negligible again.

These results show that the resolution of CL images is strongly dependent on the distribution of the generation function. Since this technique employs the Monte Carlo scheme for the generation of the distribution of the e-h pairs, it is likely to be more accurate than other models using the modified Gaussian approximation [8], uniform sphere generation or point source [11, 12, 13] for the generation function in this regime.

The contrast and resolution curves are replotted in Figure 6, where C(E) has been plotted against W(E). E_{max} coincides approximately with LT_{bv} of Figure 4. This means that beam energies below the occurrence of $C(E)_{max}$ will give, to a good approximation, the best resolution. It is interesting to note that there are cases where the values of W(E) are much smaller than L such as in d = 0.2 μm to 0.6 μm when E < LT_{bv} (Fig. 4).

Effect of defect strength

Computation was carried out to determine the effect

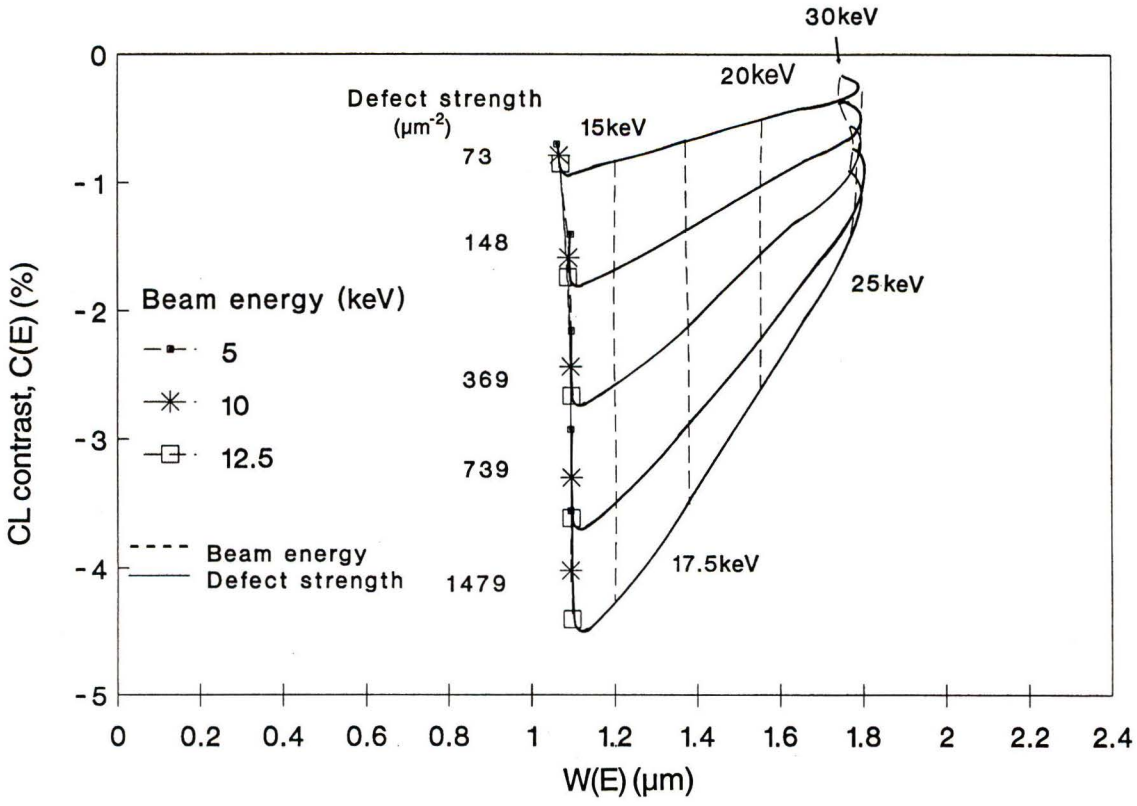

Figure 7. Plot of C(E) versus W(E) of point defects for different defect strengths; Wd → 0 μm and d = 0.8 μm. Other relevant parameters are $\theta_o = 0°$, $\delta = 0$ μm, $V_s \rightarrow \infty$, L = 1 μm and $\alpha = 0.1$ μm^{-1}.

of $\gamma(r)$ on C(E) and W(E). Figure 7 shows the computational results for a GaAs semiconductor. In this particular example, the depth of the point defect was fixed at 0.8 μm and the values of $\gamma(r)$ were varied from 73 μm^{-2} to 1479 μm^{-2}; this corresponds to the ratio of τ_r'/τ_{nr}' in the range from 100 to 2000.

One of the prominent effects of $\gamma(r)$ on the CL image is that the magnitude of C(E) increases with $\gamma(r)$. However, the shape of the curves is quite insensitive to $\gamma(r)$ and remains almost unchanged from 5 keV to 30 keV. Another important observation from the curves is that the energy at which $C(E)_{max}$ occurs is independent of $\gamma(r)$. In this case, $E_{max} \approx 12.5$ keV, the same as that in Figure 6. The observations made from Figure 4, i.e., E_{max} coincides with LT_{bv} are still valid for changing $\gamma(r)$. In addition, the variations in $C(E)_{max}$ at 12.5 keV are quite significant and range from 0.85% for $\gamma(r) = 73$ μm^{-2} to 4.4% for $\gamma(r) = 1479$ μm^{-2}.

Effect of defect size

The size of the defect is incorporated by putting $\gamma_{oi} > 0$ μm^{-2} to more nodes in the finite difference scheme spatially. Figure 8 illustrates one of the models used to approximate a small localized defect. The defect is divided into elementary volumes, each being defined by the eight nodes at its corners and characterized by a local $\gamma(r)$. Wd_x, Wd_y and Wd_z are the actual defect

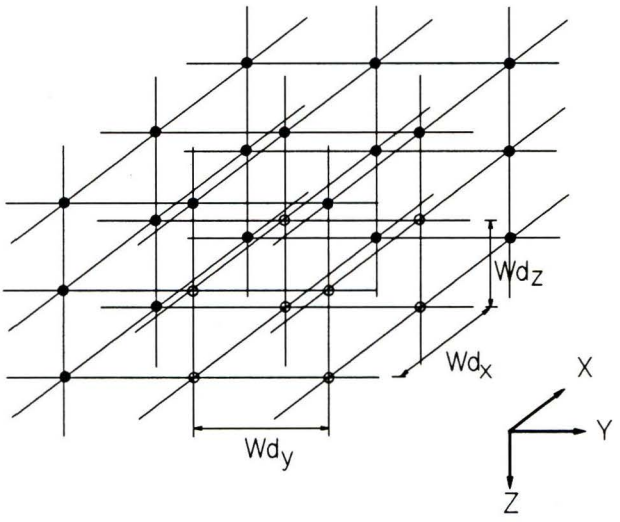

Figure 8. Model used to simulate small subsurface localized defect. ○ are nodes with $e_{oi} = 1$ and $\gamma_{oi} \neq 0$ μm^{-2} and ● are nodes with $e_{oi} = 0$ and $\gamma_{oi} = 0$ μm^{-2}.

mensions in the X-, Y- and Z-directions respectively. In this work, these dimensions are set to be equal and represented by Wd.

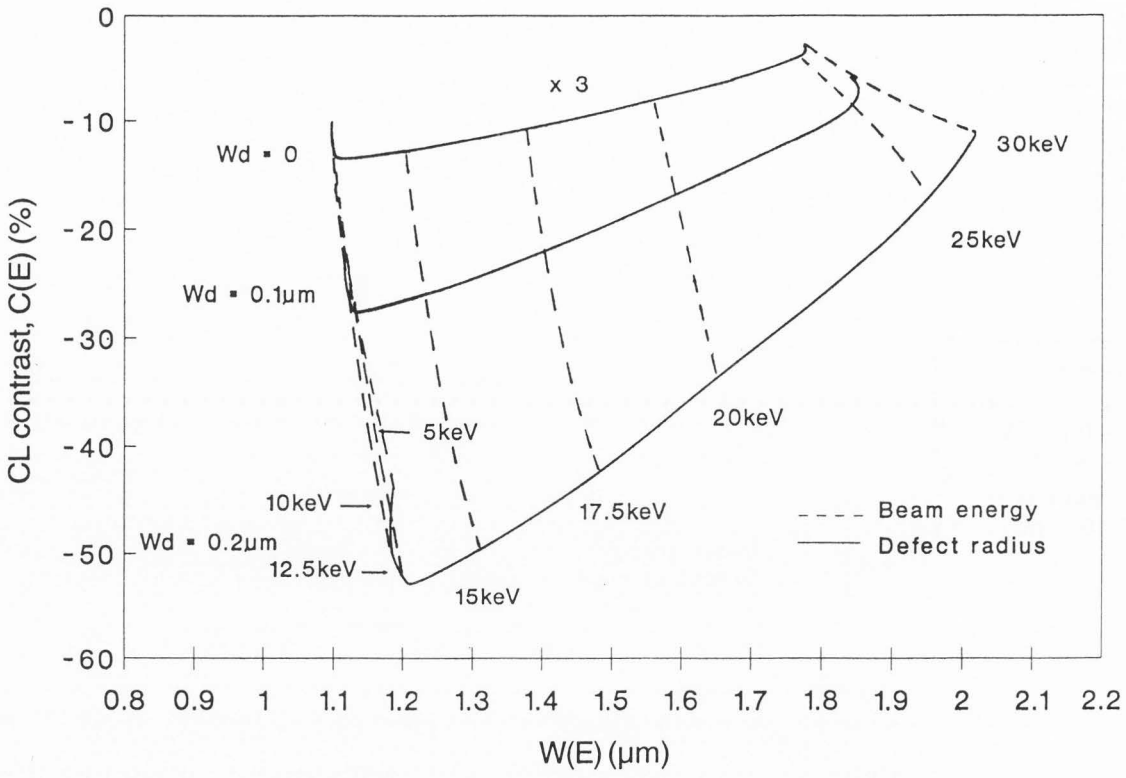

Figure 9. Plot of C(E) versus W(E) of point defects for different defect sizes; d = 0.8 μm and $\gamma(r) = 1479\ \mu m^{-2}$.

Figure 9 shows the simulated results. CL contrasts are computerized for localized defects with Wd = 0 μm, 0.1 μm and 0.2 μm. Other parameters for which calculations have been performed are the same as those for Figures 6 and 7. The following observations are made:

(1) C(E) increases with increasing Wd for all the energies. However, the contrast profiles maintain the same properties as before. Even when Wd is varied, $C(E)_{max}$ of each of the curves still appears at E_{max} = 12.5 keV;

(2) On the other hand, the range over which the contrast fluctuates is larger for bigger values of Wd. This means that larger localized defects produce a better discrimination in the C(E) profiles;

(3) For E < 12.5 keV, i.e., R_p < d (see Fig. 4 curve 5), the shift in W(E) for increasing Wd in this energy range is purely due to the effect of Wd since W(E) is quite independent of R_p and d is fixed. For E > 12.5 keV, i.e., R_p > d, the broadening effect of W(E) must take into account R_p which means that the change in W(E) is due to the increase in both Wd and R_p.

Dependence of Contrast Profiles on Beam Parameters

One of the strengths of the Monte Carlo method is that it allows the study to be extended to the dependence of CL contrast on electron beam conditions. The size and incident angle of the electron beam are the parameters of interest.

Effect of incident beam angle

Figures 10a, 10b, and 10c show how the CL contrast profiles depend on the incident beam angle at 20 keV. This is a series of graphs for point defects located at three depths (d = 0.2 μm, 0.8 μm and 2.0 μm). Linescan contrast profiles across the defects for the beam moving from the positive Y-axis into the negative Y-axis are compared for various incident beam angles. For $\theta_o = 0°$ the C(t,E) curves are symmetrical with C(E) at t = 0. The contrast profiles at $\theta_o > 0°$, however, exhibit a different behaviour. The maximum contrasts appear at different positions. With increasing values of θ_o, the maximum contrast becomes more distant from the origin. This is an important observation. For an SEM observer comparing CL micrographs, the details may seem to be displaced. This effect becomes more pronounced at higher angles.

The influence of θ_o on C(E), W(E) and the amount of offset of C(E) from t = 0, denoted by $O(E,\theta_o)$, has been summarized in Figures 11a, 11b, and 11c. The following points can be made:

(1) For d = 0.2 μm << R_p (Fig. 10a), C(E) is a slow decreasing function of θ_o. On the contrary, W(E) and $O(E,\theta_o)$ increase almost linearly with θ_o. Hence, an observer will see not only a reduction and shift in the peak contrast but also a decrease in resolution in the CL micrographs. In this range, the defect is close to the

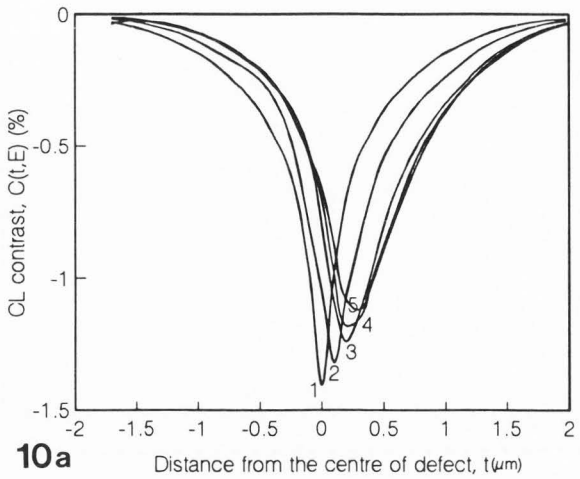

10a

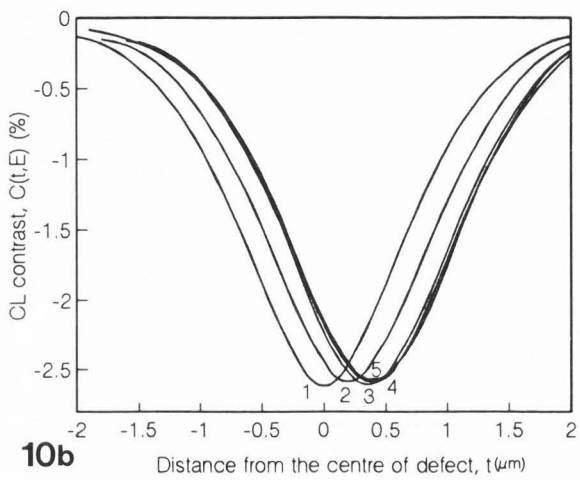

10b

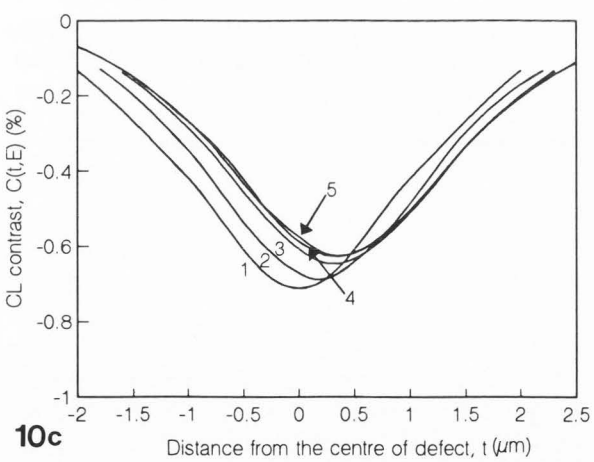

10c

Figure 10. CL contrast profiles for different incident beam angles, curve (1) $\theta_o = 0°$ (2) $\theta_o = 30°$ (3) $\theta_o = 60°$ (4) $\theta_o = 70°$ (5) $\theta_o = 80°$. (a) for d = 0.2 μm (b) d = 0.8 μm (c) d = 2.0 μm. Other relevant parameters are $\delta = 0$ μm, $V_s \rightarrow \infty$, L = 1 μm, $\alpha = 0.1$ μm^{-1}, $\gamma = 1479$ μm^{-2}.

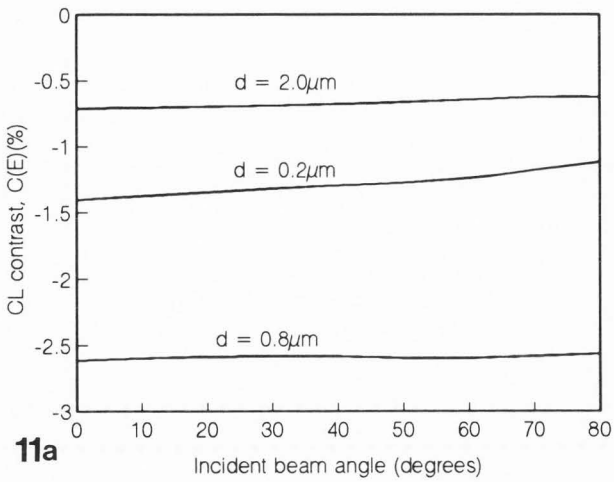

11a

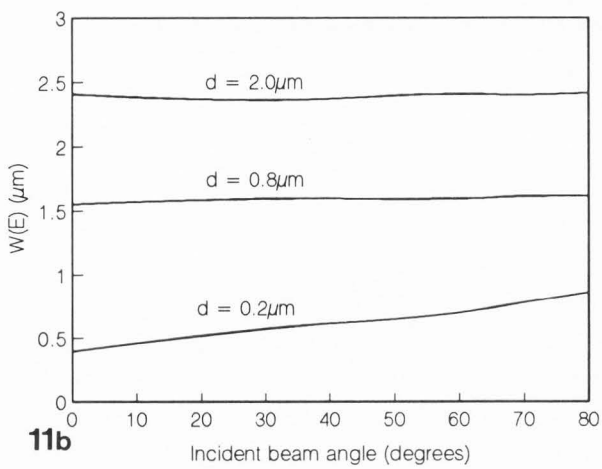

11b

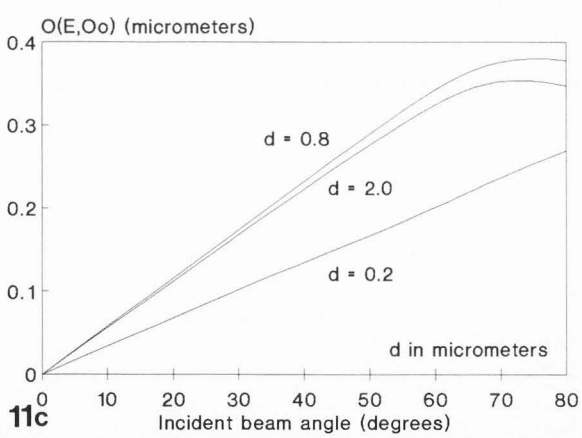

11c

Figure 11. Effect of the incident beam angle on (a) C(E) (b) W(E) (c) $O(E,\theta_o)$ for three different values of d. At $\theta_o = 0°$, R_p is approximately 2.05 μm for a 20 keV electron beam (see Fig. 4).

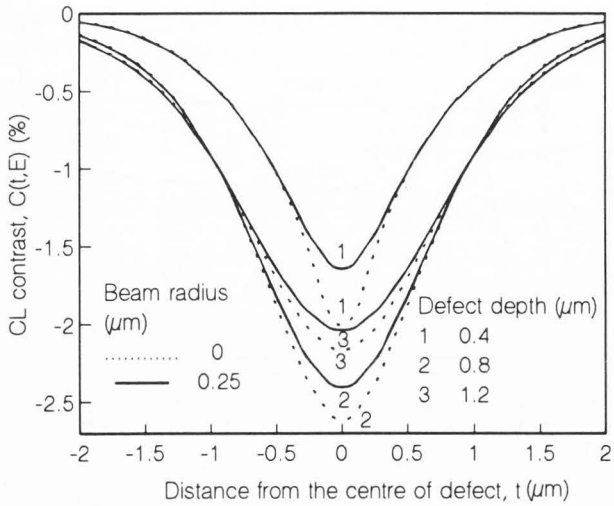

Figure 12. Effect of the beam size on the CL contrast profiles. Other relevant parameters are $\theta_o = 0°$, $V_s \rightarrow \infty$, $L = 1\mu m$, $\alpha = 0.1\mu m^{-1}$ and $\gamma(r) = 1479\mu m^{-2}$ for the point defect.

---

maximum energy dissipation positions of the incident electrons;

(2) For $d = 0.8\ \mu m \approx 1/3R_p$ (Fig. 10b), **C**(E) and **W**(E) do not change much for increasing θ_o. However, **O**(E,θ_o) has a very different response from that of $d << R_p$; the peak contrast will first move away from the origin until θ_o reaches 70° and then it turns back to the origin slightly for high values of θ_o; and

(3) For $d = 2.0\ \mu m >> 1/3R_p$ (Fig. 10c), both **C**(E) and **W**(E) decrease slowly with θ_o and saturate at 70°. Responses of **O**(E,θ_o) are the same as those for $d \approx 1/3R_p$.

Effect of beam size

The electron beam size has a significant effect on the e-h pair generation volume. It is, in fact, the dominant factor in deciding the CL image quality. Figure 12 illustrates **C**(t,E) profiles for values of the radius of the incident electron beam, $\delta = 0\ \mu m$ and $0.25\ \mu m$ at 20 keV. There are two main influences associated with increasing the beam size. It lowers the contrast around the defect and it broadens **W**(E) considerably. These lead to a diffused CL image with low contrast range. With reference to Figure 13, it is evident that these two effects become more pronounced at higher values of θ_o.

Determination of Defect Properties

Determination of defect depth

Based on the results of the plots of **C**(E) versus **W**(E) in Figures 6, 7 and 9, it is very interesting to see that E_{max} is a function only of d and insensitive to the

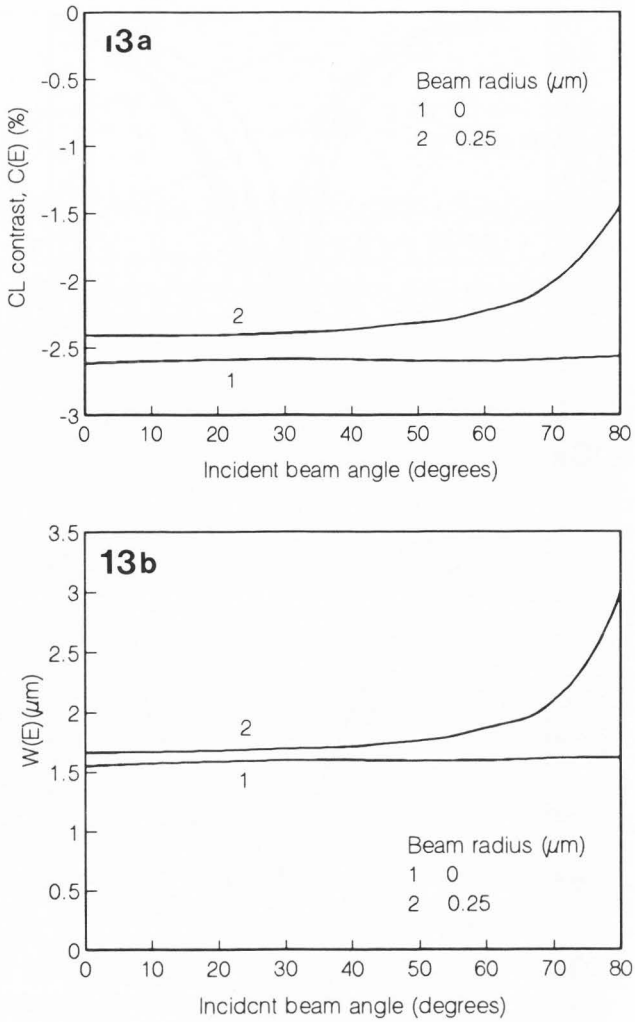

Figure 13. Effect of the beam size on (**a**) **C**(E) (**b**) **W**(E) for different incident beam angles.

---

variations in $\gamma(r)$ and Wd. As a result, one is able to determine d based on the data such as those shown in Figures 2 and 3. As an application of these observations, the plot shown in Figure 14 was constructed. This plot, based on the locus of Figure 3, relates the defect d to E_{max}. The equations shown in Figure 14 were determined by a least square polynomial curve fitting technique. They show the range of estimated depth for E_{max} up to approximately 30 keV. This method has been applied to determine the depth of subsurface dislocations in GaAs and the work can be found in Pey *et al.* [15].

Suppose $C(E)_{max}$ is observed from the CL image or from line-scan profiles across a defect at E_{max}; the depth of the defect is then obtained by substituting E_{max} into one of the equations in Figure 14. The precision of this evaluation depends on the observer's ability to detect the

variations of image or contrast profile with beam energy. The depth resolution of this method is very much dependent upon the contrast discrimination level especially for beam energies near the E_{max} and will be worse for deeper defects since the contrast decreases rapidly (see Fig. 3).

Determination of defect size

Another potential application of the C(E) versus W(E) contour plots of Figures 6, 7 and 9 is the determination of defect size. If d is measured independently by the method mentioned in the previous section, the defect size can be extracted from the theoretical data points using W(E) for beam energies $\leq E_{max}$, since it has been demonstrated in Figures 7 and 9 that W(E) in this energy range is only a function of defect size and independent of $\gamma(r)$.

Suppose one performs line-scan measurements and observes constant W(E) of the images below E_{max}; the size of the small localized defect is then measured by a best fit of the experimental value of W(E) to the portion of the curves with beam energies that are below E_{max} in Figure 9. For a given d value, the "size resolution" is improved for larger defect.

Determination of defect strength

The local recombination activities of the defect can be effectively measured if d and Wd are known. Given a set of values for d and Wd, which are measured separately by the approaches mentioned previously, $\gamma(r)$ can be determined by matching the experimental C(E) versus W(E) data points to the series of curves shown in Figure 7. Within the framework of this model, the details inside of the small defect cannot be analyzed since the obtained value for $\gamma(r)$ is assumed to be uniform throughout the defect structure.

Figure 15 summarizes all the necessary steps to measure the three defect parameters effectively for a set of CL contrast from a small localized defect.

Effect of a Dislocation on Cathodoluminescence Contrast

An example of an extended defect is a dislocation which intersects the surface perpendicularly at t = 0. The recombination properties of dislocations are due to either the inherent structure of the dislocation [18] (e.g., dangling bonds or reconstructed dangling bonds in the dislocation core), or due to the Cottrell atmosphere of point defects around the dislocation. As in the case of charged lines surrounded by an electric field, the exact analysis would require taking into account the drift component of the dislocation cylinder [11]. In the approximation applied here, a pure diffusion mechanism was assumed both inside and outside the dislocation cylinder.

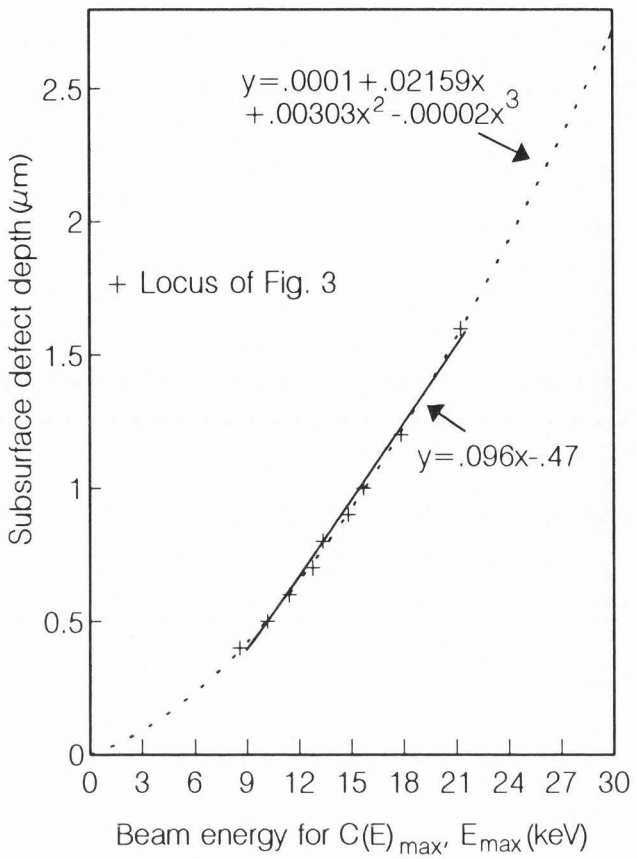

Figure 14. The depth of a subsurface point defect as a function of beam energy for $C(E)_{max}$. Two approximations over different ranges of interest are given.

Similar to the definition of small defect size, the dislocation is divided into elementary segment of length, e.g., Wd_z and cross section Wd_x Wd_y. Each segment is defined by the eight nodes at its corners, and characterized by a local value of $\gamma(r)$. An extended dislocation is then considered to be the sum of all the elementary elements in one particular direction.

Figure 16 shows an example for CL contrast at various beam energies for a GaAs sample having a very fine threading dislocation intersecting perpendicularly with the top surface with both Wd_x and $Wd_y \rightarrow 0$. W(E) of the curves increases very rapidly with E. On the other hand, C(E) of each profile is a strong decreasing function of E. The contrast response of a dislocation (Fig. 16) differs considerably from those of a point defect (Fig. 2).

The CL contrast of a threading dislocation perpendicular to the top sample surface is a decreasing function of beam energy which is similar to the EBIC contrast profiles reported by Donolato [7], whereas the contrast of a subsurface defect has a minimum at a particular

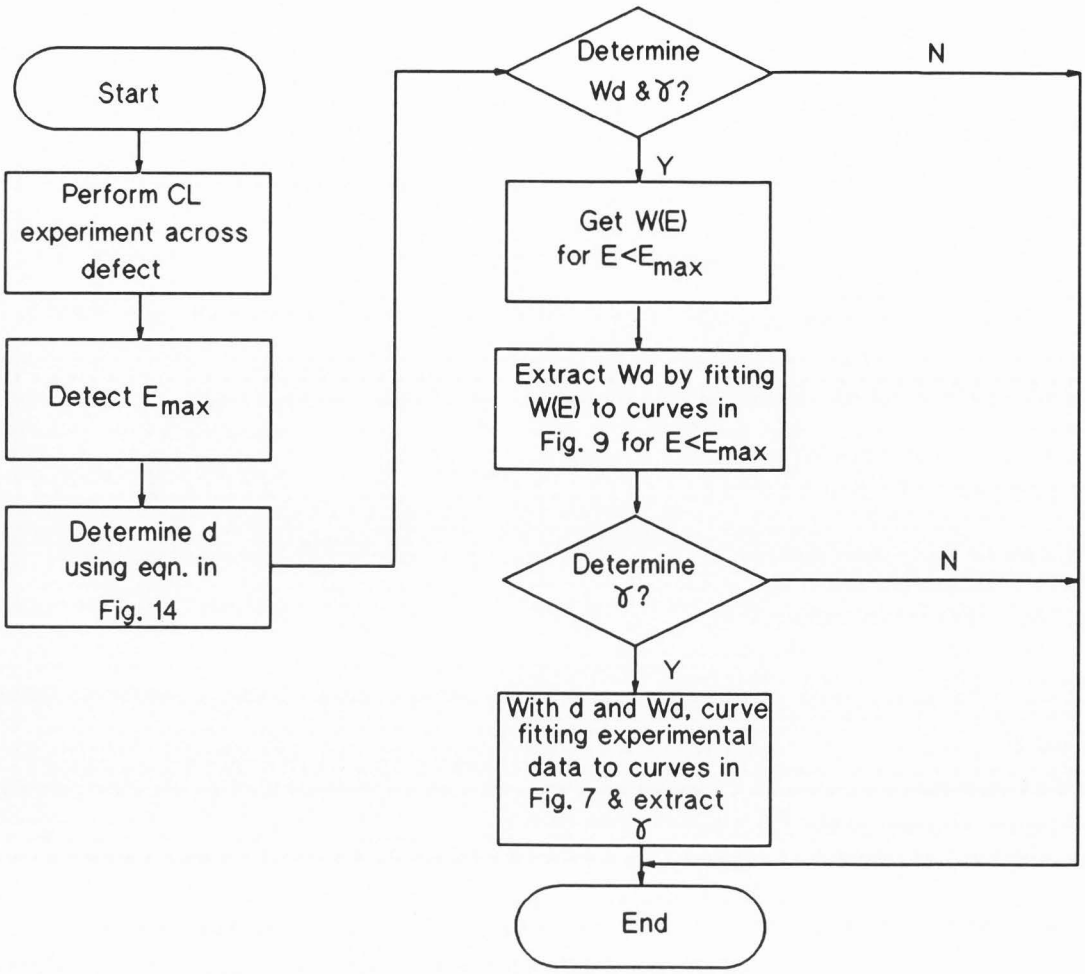

Figure 15. Flow chart for determining the defect parameters.

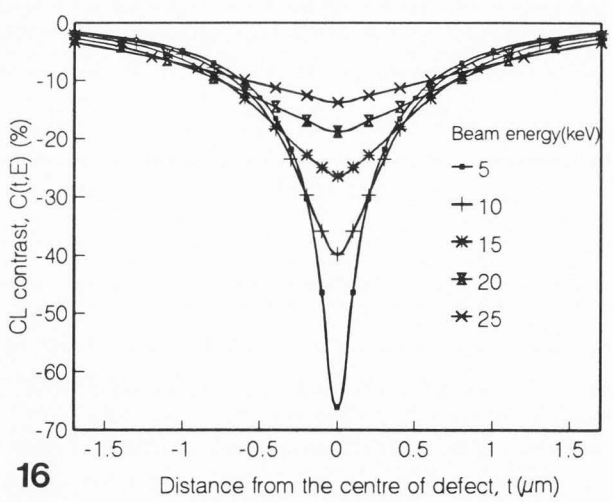

Figure 16. CL contrast profiles for various values of beam energies for a straight threading dislocation perpendicular to the surface in GaAs. Other relevant parameters for this model are $\theta_o = 0°$, $\delta = 0$ μm, $V_s \rightarrow \infty$, $L = 1$ μm, $\gamma(r) = 1479$ μm^{-2} and $\alpha = 0.1$ μm^{-1}.

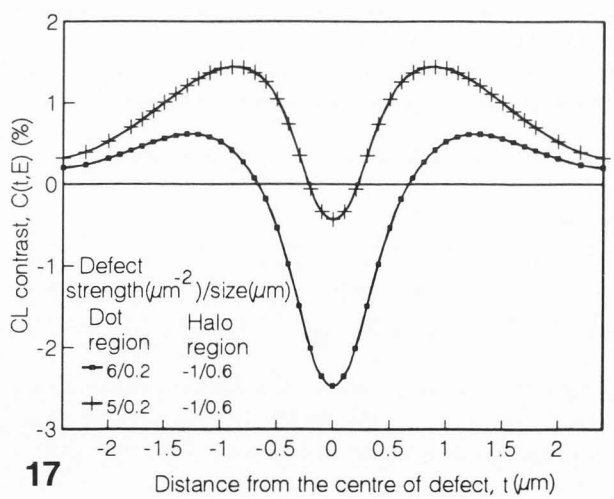

Figure 17. Dot and halo responses simulated at 20 keV. Other relevant parameters are $\theta_o = 0°$, $\delta = 0$ μm, $V_s \rightarrow \infty$, $L = 1$ μm and $\alpha = 0.1$ μm^{-1}.

energy. Identification of these two imperfections can hence be carried out easily using the different CL contrast behaviour. One can perform line-scan experiments or simply observe the contrast responses at different beam energies across the defect of interest. If the dark spot is present at all beam energies or if contrast features similar to Figure 16 are observed, it corresponds to a line defect penetrating into the bulk materials. If it appears very clearly only at a fixed beam energy or contrast features similar to Figure 2 are found, it is a subsurface localized bulk defect.

Simulation of "Dot-and-Halo" Cathodoluminescence Contrast

When a dislocation is viewed end on, several different forms of CL images have been observed: dark dot, bright dot and dot-and-halo contrast [18]. Of these three types of contrasts, the dot-and-halo response is the most interesting one. It has been reported by many workers [1, 17] that the contrast is due to the variations in doping concentration around dislocation in Te- and Se-doped GaAs. Another mechanism that may be responsible for the observation of dot-and-halo contrast in GaP substrate [4, 5] is the gettering effect of the dislocation. As a result, there is a reduction in the local concentration of non-radiative centres leading to local CL enhancement. The effect of the second mechanism can be easily modelled by assuming that there is a decrease and increase in local τ'_{nr} within and around the dislocation cylinder respectively. The increase in τ'_{nr} around the dislocation can be seen as a reduction in non-radiative centres and the local $\gamma(r)$ is made to be less than zero. Two contrast profiles were simulated. The model assumed that the dot and halo regions of each of the contrast profiles have a size of 0.2 μm and 0.6 μm respectively. However, the $\gamma(r)$ of the dot and halo regions were set to 6 μm^{-2} and -1 μm^{-2} for the first contrast and 5 μm^{-2} and -1 μm^{-2} for the second. The numerical results are shown in Figure 17.

Conclusions

The representation of the continuity equation by its numerical equivalence in the CL Model is useful in modelling of multiple or complex defects because the approach does not require the knowledge of the mathematical expressions for the defect of interest. The contrast of cathodoluminescence images of small localized defects, threading dislocation and dot-and-halo response in semiconductors have been investigated. It was found that the resolution of the CL image is particularly sensitive to the defect depth and size, whereas the contrast is a function of all the defect parameters including the "defect strength." The image contrast responses and resolutions also vary nonlinearly with the beam diameter and specimen tilt. Image contrast of threading dislocation exhibits a decreasing function of beam energy, whereas for subsurface defect, a contrast reversal can be observed. A simple method of distinguishing the two defects has been established. Based on the different effects of defect parameters on contrast behaviours, the depth, size and strength of bulk localized defects can be extracted sequentially using the computer model.

Acknowledgements

Research funding from the National University of Singapore under Research Project RP900614 is acknowledged. One of the authors, KL Pey, gratefully acknowledges the support given by National University of Singapore through a Research Scholarship.

References

[1] Balk LJ, Kubalek E, Menzel E (1976) Investigations of as-grown dislocations in GaAs single crystals in the SEM. Scanning Electron Microsc. **I**:257-264.

[2] Booker GR (1981) Developments in semiconducting material applications of the SEM, In: Microscopy of Semiconducting Materials. Cullis AG and Joy DC (eds.). Institute of Physics, Bristol. pp. 203-214.

[3] Czyżewski Z and Joy DC (1990) Monte Carlo simulation of CL and EBIC contrasts for isolated dislocations. Scanning **12**, 5-12.

[4] Darby DB and Booker GR (1977) Scanning electron microscope EBIC and CL micrographs of dislocations in GaP. J. Mat. Science **12**, 1827-1833.

[5] Davidson SM, Iqbal MZ, Northrop DC (1975) SEM cathodoluminescence studies of dislocation recombination in GaP. Phys. Stat. Sol. **a29**, 571.

[6] Donolato C (1978) On the study of SEM charge-collection imaging of localized defects in semiconductors. Optik **52**, 19-36.

[7] Donolato C (1979) Contrast and resolution of SEM charge-collection images of dislocations. Appl. Phys. Lett. **34**, 80-81.

[8] Hergert W, Reck P, Pasemann L, Schreiber J (1987) Cathodoluminescence measurements using the scanning electron microscope for the determination of semiconductor parameters. Phys. Stat. Sol. **a101**, 611-618.

[9] Holt DB and Saba FM (1985) The cathodoluminescence mode of the scanning electron microscope: A powerful microcharacterization technique. Scanning Electron Microsc. **III**, 1023-1045.

[10] Jakubowicz A (1985) On the theory of electron-beam-induced current contrast from point-like defects in semiconductors. J. Appl. Phys. **57**, 1194-1199.

[11] Jakubowicz A (1986) Theory of cathodoluminescence contrast from localized defects in semiconductors. J. Appl. Phys. **59**, 2205-2209.

[12] Löhnert K and Kubalek E (1984) The cathodoluminescence contrast formation of localized non-radiative defects in semiconductors. Phys. Stat. Sol. **a83**, 307-314.

[13] Pasemann L (1981) A contribution to the theory of the EBIC contrast of lattice defects in semiconductors. Ultramicroscopy **6**, 237-250.

[14] Pasemann L and Hergert W (1987) EBIC and cathodoluminescence contrast due to individual dislocations. Izvestiya Akademii Nauk SSSR. Seriya Fizicheskaya **51**, 1528-1534.

[15] Pey KL, Phang JCH, Chan DSH (1993) Investigation of dislocations in GaAs using cathodoluminescence in the scanning electron microscope. Scanning Microsc., **54**, 1195-1206.

[16] Phang JCH, Pey KL, Chan DSH (1992) A simulation model for cathodoluminescence in the scanning electron microscope. IEEE Trans. Electron Devices **39**, 782-791.

[17] Shaw DA and Thornton PR (1968) Cathodoluminescent studies of laser quality GaAs. J. Mat. Science **3**, 507-518.

[18] Yacobi BG and Holt DB (1990) Applications In: Cathodoluminescence Microscopy of Inorganic Solids. Plenum Press, New York. pp. 121-164

Discussion with Reviewers

J.F. Breese: In your calculations of the contrast, you are assuming that there is no variation of the radiative lifetime inside the defect zone. This assumption may be applied for a dislocation core but not for a Cottrell atmosphere where the impurity concentration changes the radiative lifetime (directly related to the impurity concentration). By this fact, it seems difficult to apply your model to the "dot and halo" contrast. Please comment.
Authors: In the simulation of the "dot and halo" contrast, we assumed that there is only a variation in the non-radiative lifetime within the defect zones. For simulation of Cottrell atmosphere, the change in the radiative lifetime due to the spatial variation in the impurity concentration can be modeled through the defect parameter $\gamma(r)$ of eq. (3) in Part I which, in turn, is controlled by the lifetimes in eqs. (4) and (5) of Part II. In this model, $\gamma(r)$, τ and τ' of the numerical equations at different nodes can be varied to model a spatially varying lifetime, such as τ_r and τ'_r.

J.F. Breese: When you are talking about a spatial resolution better than the diffusion length, it may be true for the defect imaging, but for imaging different layers the spatial resolution is mainly governed by the diffusion length. Can you clarify this point?
Authors: Donolato (1978) has shown that in the calculation of the minority carrier density distribution for EBIC, even for the case for a very large L (tending to infinity), the volume where the minority carrier density is significant is the same order of magnitude as the volume of the generation sphere. This shows that the common assumption that the carrier diffusion length determines the volume in which the carriers spread is not justified. Based on this observation, we do not think that the resolution for CL imaging of different layers is governed mainly by the diffusion length. Also in CL imaging of different layers, the contrast is caused by differences in quantum efficiency and absorption coefficient among other factors.

J.F. Breese: It seems not evident to go back to the defect width only using the FWHM value of the CL profiles, using the curves of Figure 9, especially when you are working at an energy below 15 keV. Can you give an estimation of the accuracy?
Authors: Based on our simulation results, for beam energies $\leq E_{max}$, W(E) remains fairly constant for a given defect size and is independent of the defect strength $\gamma(r)$ (see Fig. 7). Pey *et al.* (1993) have demonstrated that good CL contrast of dislocations can be obtained using a lock-in method even at low electron beam energies (see Figs. 4a, 6b and 7b of Pey *et al.*, 1993). We believe that it is still possible to extract the information on W(E) with high accuracy at low beam energies if the operating conditions are adjusted properly.

S. Myhajlenko: In your descriptions of the behaviour of C(E), W(E), O(E), etc. you have assumed (realistically) for GaAs that the surface recombination velocity (v_s) is very high (experimentally $\approx 10^7$ cm/s). For a given L, the defect depth is the determining parameters as you vary beam voltage. What would you expect the major effect of a lower surface recombination velocity to be on your contrast behaviour model? Such a case would apply to InP, for instance, $v_s = 10^3$-10^4 cm/s. Would you still have the four regions of behaviour?
Authors: The effect of the surface recombination velocity can be viewed as a sink of excess minority carriers at the top surface. If the strength of v_s is uniform throughout the surface, the effect of changing v_s will be similar to the effect of changing the strength, $\gamma(r)$, of a localised defect as shown (Fig. 7), except that now all the non-radiative combination centres are situated at the top surface, i.e., z = 0 μm. Based on this deduction, we predict that there will still be a maximum contrast for a localised defect at E_{max} in the beam energy dependent CL contrast and will still have the four regions of behaviour in the W(E) versus beam energy plot (Fig. 4).